Heliyon 10 (2024) e32719

Contents lists available at ScienceDirect

Heliyon

journal homepage: www.cell.com/heliyon

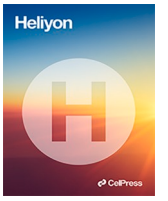

Research article

Microwave-assisted synthesis of Ni-doped europium hydroxide for photocatalytic degradation of 4-nitrophenol

Shaidatul Najihah Matussin [a], Fazlurrahman Khan [b,c,d], Mohammad Hilni Harunsani [a], Young-Mog Kim [c,d,e], Mohammad Mansoob Khan [a,*]

[a] Chemical Sciences, Faculty of Science, Universiti Brunei Darussalam, Jalan Tungku Link, Gadong, BE 1410, Brunei Darussalam
[b] Institute of Fisheries Science, Pukyong National University, Busan 48513, Republic of Korea
[c] Marine Integrated Biomedical Technology Center, The National Key Research Institutes in Universities, Pukyong National University, Busan, 48513, Republic of Korea
[d] Research Center for Marine Integrated Bionics Technology, Pukyong National University, Busan, 48513, Republic of Korea
[e] Department of Food Science and Technology, Pukyong National University, Busan, 48513, Republic of Korea

ARTICLE INFO

Keywords:
Europium hydroxide
$Eu(OH)_3$
Nickel-doped $Eu(OH)_3$
Nanorods
Photocatalysis
4-nitrophenol
Pseudo-first-order reaction

ABSTRACT

Microwave-assisted synthesis method was used to prepare europium hydroxide ($Eu(OH)_3$) and different percentages of 1, 5, and 10 % nickel-doped $Eu(OH)_3$ (Ni–$Eu(OH)_3$) nanorods (NRs). X-ray diffraction study showed a hexagonal phase with an average crystallite size in the range of 21 – 35 nm for $Eu(OH)_3$ and Ni–$Eu(OH)_3$ NRs. FT-IR and Raman studies also confirmed the synthesis of $Eu(OH)_3$ and Ni–$Eu(OH)_3$. The synthesized materials showed rod-like morphology with an average length and diameter between 27 – 50 nm and 8 – 13 nm, respectively. The band gap energies of Ni–$Eu(OH)_3$ NRs were reduced (4.06 – 3.50 eV), which indicates that the doping of Ni^{2+} ions has influenced the band gap energy of $Eu(OH)_3$. The PL study exhibited PL quenching with Ni doping. The photocatalytic degradation of 4-nitrophenol (4-NP) by the synthesized materials under UV light irradiation was investigated, in which 10 % Ni–$Eu(OH)_3$ NRs showed the best response. A kinetic study was also conducted which shows pseudo-first-order kinetics. Based on this, Ni–$Eu(OH)_3$ NRs have shown a potential to be a UV-light active material for photocatalysis.

1. Introduction

In general, nanomaterials show excellent optical, electronic, magnetic, and mechanical properties owing to their unique small size, surface, and quantum effects. These materials have been widely applied in catalysis [1–3], environment [4], biomedicine [5], energy [6], etc. Their size, crystal form, and morphology determine the physical and chemical properties of nanomaterials, in which materials with the same chemical composition may show different properties if the materials have differences in their characteristics [7–11]. These materials could be 0D, 1D, 2D, or 3D [12].

Europium hydroxide ($Eu(OH)_3$) exhibit electronic, optical, catalytic, and chemical properties that arise from electron transitions within the 4*f* shell [7,13,14]. Many studies have been made to synthesize $Eu(OH)_3$ using various methods, for instance, Zeng et al. synthesized $Eu(OH)_3$ nanorods *via* hydrothermal method at 150 °C for 24 h [15]. Short, rod-like morphology have been acquired with a

* Corresponding author.
E-mail addresses: mmansoobkhan@yahoo.com, mansoob.khan@ubd.edu.bn (M.M. Khan).

https://doi.org/10.1016/j.heliyon.2024.e32719
Received 18 March 2024; Received in revised form 4 May 2024; Accepted 23 May 2024
Available online 8 June 2024

diameter of around 140 nm and lengths between 100 and 500 nm. Similarly, Lie et al. prepared $Eu(OH)_3$ nanorods using the same synthesis method at 160 °C [13]. However, in this case, cationic CTAB was used. $Eu(OH)_3$ nanorods of 450 nm in length and 10–30 nm in diameter were obtained. Patra et al. synthesized $Eu(OH)_3$ using a microwave-assisted method [16]. Rod-like $Eu(OH)_3$ was obtained which were 200–300 nm in length and 35–50 nm in diameter. Zhang et al., also prepared $Eu(OH)_3$ nanoclusters through microwave assisted-hydrothermal at 150 °C and 150 W for 10 min [17]. The $Eu(OH)_3$ nanoclusters were composed of approximately 5 nm Eu $(OH)_3$ NPs.

p-nitrophenol (4-nitrophenol, 4-NP) is known to be anthropogenic and inhibitory in nature in which at high concentrations, it would be difficult to mineralize or degrade [18]. Untreated water with this contaminant might result in adverse effects to both human beings and animals, which include severe vomiting, headaches, and organ failure such as the liver, kidney, and central nervous systems [2]. Moreover, due to its stability and high solubility, it might also result in ecological stress. Therefore, researchers have developed materials for the degradation of 4-NP [19–21].

As per the authors' knowledge, the synthesis of Ni-doped $Eu(OH)_3$ nanorods (NRs) using the microwave-assisted synthesis method has not been reported. Ni^{2+} as a dopant has shown enhanced photocatalytic degradation of pollutants [22,23]. Therefore, in this study, the microwave-assisted synthesis method was employed for the first time to synthesize Ni-doped $Eu(OH)_3$. In order to study the influence of Ni-doping, the structural, optical, and morphological properties of $Eu(OH)_3$ and Ni–$Eu(OH)_3$ NRs were studied using various characterization techniques. Moreover, the activity of $Eu(OH)_3$ and Ni–$Eu(OH)_3$ NRs as photocatalysts were also investigated for the photocatalytic degradation of 4-NP, which is a colourless pollutant, under UV light irradiation for 5 h.

2. Experimental

2.1. Chemicals used

Europium acetate hydrate ($Eu(CH_3COO)_3{\cdot}H_2O$, 99 %) and nickel (II) nitrate hexahydrate ($Ni(NO_3)_2{\cdot}6H_2O$, 99 %) were obtained from Alfa-Aesar and Acros, respectively. Sodium hydroxide (NaOH, 99.9 %) was obtained from Merck. Throughout the experiments, water was purified using Aquatron (England). For the photocatalysis experiment, 4-nitrophenol ($C_6H_5NO_3$, 99 %) was used and obtained from Merck. For the trapping experiments, isopropanol and benzoquinone were obtained from Acros.

2.2. Instruments used

X-ray diffraction ((XRD) Shimadzu XRD-7000 X-ray diffractometer) was used to investigate the structural properties of $Eu(OH)_3$ and Ni–$Eu(OH)_3$ with Cu Kα radiation ($\lambda = 1.5418$ Å). Raman spectra of the samples were analyzed using a Raman spectrophotometer (NRS-5100, JASCO) at a laser wavelength of 785 nm. The presence of vibrational modes of $Eu(OH)_3$ and Ni–$Eu(OH)_3$ was studied using Fourier Transform-Infrared Spectroscopy (FT-IR, Shimadzu IRPrestige-21 Fourier Transform-Infrared Spectrophotometer) from 450 to 4000 cm^{-1}. Field emission transmission electron microscopy (FE-TEM) was utilized to analyze the morphology of the materials and the selected area electron diffraction (SAED) was conducted with JEM-F200 (JEOL Ltd., Tokyo, Japan). A photoluminescence (PL) study of $Eu(OH)_3$ and Ni–$Eu(OH)_3$ was carried out using F-7000 Fluorescence spectroscopy (Hitachi High Tech) at an excitation wavelength of 370 nm. The band gap energies of $Eu(OH)_3$ and Ni–$Eu(OH)_3$ were determined using UV–Vis diffuse reflectance spectroscopy (DRS) (Shimadzu, UV-2600). X-ray photoelectron spectroscopy (XPS) of the synthesized materials was performed on Kratos Analytical, AXIS Nova. The photocatalytic degradation of 4-NP was conducted using a photochemical reactor (Toption, TOPT-V) irradiated by a 300 W UV lamp. The absorbance of 4-NP and the reaction solution were monitored using a UV–visible spectrophotometer (Shimadzu UV-1900, Japan).

2.3. Microwave-assisted synthesis of $Eu(OH)_3$ NRs

Microwave-assisted synthesis method was used to prepare $Eu(OH)_3$ NRs according to the literature [24]. In short, Eu $(CH_3COO)_3{\cdot}H_2O$ solution (0.05 M) was prepared in a microwave vessel prior to the addition of 2.4 mL of 1 M NaOH into the prepared solution. The solution was heated slowly to 180 °C for 10 min in the microwave reactor with stirring and it was maintained at 180 °C for 15 min at 850 W microwave power. The obtained product was centrifuged and washed three times with distilled water. It was dried at 80 °C in the oven before it was ground to produce $Eu(OH)_3$ powder.

2.4. Microwave-assisted synthesis of Ni–$Eu(OH)_3$ NRs

Ni–$Eu(OH)_3$ NRs were synthesized using the same method as mentioned above. In brief, a specific amount of $Ni(NO_3)_2{\cdot}6H_2O$ (1, 5, and 10 % Ni–$Eu(OH)_3$) was added to the 0.05 M aqueous $Eu(CH_3COO)_3{\cdot}H_2O$ solution prepared earlier. Subsequently, 1 M NaOH solution was added dropwise into the solution. The microwave reaction temperature was increased to 180 °C in 10 min and the synthesis reaction was carried out at 180 °C for 15 min at 850 W microwave power. The product was obtained by centrifuging, washed three times with distilled water and then dried at 80 °C. The obtained products were coded as 1 % Ni- $Eu(OH)_3$, 5 % Ni- $Eu(OH)_3$, and 10 % Ni- $Eu(OH)_3$.

2.5. Photocatalytic degradation of 4-nitrophenol

The photocatalytic degradation of 4-NP using $Eu(OH)_3$ and 1, 5, and 10 % Ni–$Eu(OH)_3$ was investigated under UV light irradiation. $Eu(OH)_3$ and 1, 5, and 10 % Ni–$Eu(OH)_3$ NRs (10 mg) were put in 50 mL of 10 ppm 4-NP aqueous solution. It was first sonicated for 3 min and proceeded with stirring in the dark for 3 min. Then, the photocatalytic reaction was carried out with a 300 W UV light irradiation for 5 h. The absorbance of the 4-NP solution was measured at every hour. The percentage of photocatalytic degradation of 4-NP was obtained using the following equation (**Eq. 1**):

$$\%\ photocatalytic\ 4-NP\ \ degradation = \frac{(A_{blank} - A_{sample})}{A_{blank}} \times 100 \quad (1)$$

in which A_{blank} is the absorbance of 4-NP only and A_{sample} is the absorbance of 4-NP after photocatalytic degradation reaction with the respective catalyst.

2.6. Active species trapping experiment

The radical trapping experiment was conducted following the same photocatalytic degradation of the 4-NP procedure. In brief, 10 mg of 10 % Ni–$Eu(OH)_3$ was put in 50 mL of 10 ppm 4-NP aqueous solution. Exactly 500 μL of isopropanol (10 mmol/L) and benzoquinone (1 mmol/L) was added separately. Then, it was first sonicated for 3 min and proceeded with stirring in the dark for 3 min. Then, the trapping experiment was carried out with a 300 W UV light irradiation for 5 h. The absorbance of the 4-NP solution was measured at every hour and the percentage of the photocatalytic degradation of 4-NP in the presence of trapping agents was obtained using Eq. (1). The experiment was conducted in triplicates.

3. Results and discussion

3.1. X-ray diffraction

The structural properties of the synthesized $Eu(OH)_3$ and Ni–$Eu(OH)_3$ NRs were determined using powder X-ray diffraction (XRD) analysis (Fig. 1). Peaks were visible at approximately $2\theta = 16.10$, 28.08, 29.58, 32.58, and 41.04° corresponding to the (010), (110), (011), (020), and (021) planes, respectively, which are in good agreement with the literature [7,25,26]. All peaks were indexed to a pure hexagonal phase (space group = $P6_3/m$) of $Eu(OH)_3$ (JCPDS no. 98-020-0488) [27]. No impurities were observed in $Eu(OH)_3$, 1 % Ni–$Eu(OH)_3$, 5 % Ni–$Eu(OH)_3$, and 10 % Ni–$Eu(OH)_3$ NRs suggesting that the materials were successfully synthesized and Ni^{2+} ions were incorporated into the lattice. Moreover, it was observed that the peak intensity was higher in the case of 1 % Ni–$Eu(OH)_3$ NRs in comparison to $Eu(OH)_3$. However, further increase in Ni-doping concentration i.e., 5 % Ni–$Eu(OH)_3$ and 10 % Ni–$Eu(OH)_3$ has resulted in the lowering of the peak intensity. The lowering of peak intensity may be due to the difference in electron densities of Ni and Eu, which mainly depends on factors such as scattering and structure factors [28].

The average crystallite size was calculated to study the effect of doping on the structural properties of the $Eu(OH)_3$. Hence, their average crystallite size was calculated using the Debye-Scherrer's equation (**Eq. 2**):

$$D = k\lambda/\beta \cos\theta \quad (2)$$

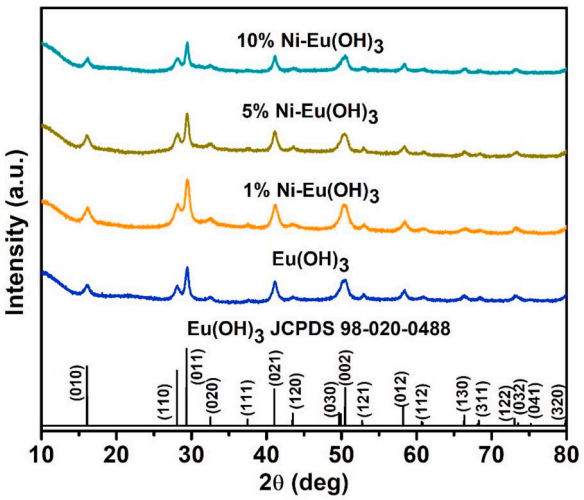

Fig. 1. XRD patterns of $Eu(OH)_3$ and Ni–$Eu(OH)_3$ NRs.

where λ represents the wavelength of the X-ray, θ indicates the Bragg angle, and β is the FWHM of the characteristic peaks. The average crystallite size of $Eu(OH)_3$ was found to be 35.84 nm. However, when 1 % and 5 % Ni were doped into the $Eu(OH)_3$ lattice, the average crystallite size was reduced greatly to 22.09 and 21.88 nm, respectively (Table 1). In the case of 10 % Ni–$Eu(OH)_3$, the crystallite size increased slightly to 24.14 nm. This might be due to the difference in the ionic radii of Eu^{3+} and Ni^{2+}. As the amount of Ni^{2+} replacing the Eu^{3+} is more than 10 %, this might lead to an increase in internal strain [29]. Moreover, the effect of Ni doping was also studied based on the average lattice strain. It was also calculated using **Eq. (3)** [30,31]:

$$\varepsilon = \frac{\beta_{hkl}}{4\ tan\ \theta} \tag{3}$$

where θ is the diffraction angle and β is the full-width half maxima (FWHM) in radians. It was found that the average lattice strain for $Eu(OH)_3$ and 1, and 5 % Ni–$Eu(OH)_3$ NRs showed no significant change (Table 1). However, 10 % Ni–$Eu(OH)_3$ showed a smaller average lattice strain value which could lead to an increase in crystallite size [29].

The lattice parameters (a and c) were calculated for $Eu(OH)_3$ and Ni–$Eu(OH)_3$ NRs and it was found that there is no significant change in the lattice parameter for the synthesized materials. Similarly, no significant difference in the cell volume was observed. This shows that there is not much distortion in the lattice of $Eu(OH)_3$ after doping with Ni^{2+} except minor changes in the average crystallite size.

3.2. Fourier transform infrared and Raman spectroscopy

The different vibrational modes of $Eu(OH)_3$, 1 % Ni–$Eu(OH)_3$, 5 % Ni–$Eu(OH)_3$, and 10 % Ni–$Eu(OH)_3$ NRs were studied using FT-IR as shown in Fig. 2(a). A vibration band of Eu-*O*-H was present at approximately 645 cm^{-1}, in all the samples [32]. The band intensity was seen to decrease as the concentration of Ni^{2+} doping increased. This might correspond to the successful doping of Ni^{2+} into the $Eu(OH)_3$ lattice. Symmetric and asymmetric stretching of O–C–O were observed in all synthesized materials at ~1394 cm^{-1} [25]. Moreover, O–H vibration at 1600 cm^{-1} was observed from the absorbed moisture on the surface of the $Eu(OH)_3$, 1 % Ni–$Eu(OH)_3$, 5 % Ni–$Eu(OH)_3$, and 10 % Ni–$Eu(OH)_3$ NRs [27]. The broad shoulder at about 3400 cm^{-1} may be ascribed to absorption of water molecules. The sharp band at ~3550 cm^{-1} was observed in $Eu(OH)_3$, 1, 5, and 10 % Ni–$Eu(OH)_3$ NRs is assigned to the coordinated O–H stretch [27].

Raman study of $Eu(OH)_3$, 1, and 10 % Ni–$Eu(OH)_3$ NRs was carried out and the respective Raman spectra are shown in Fig. 2(b). $Eu(OH)_3$ showed three obvious Raman peaks at 303.22, 377.37, and 485.83 cm^{-1}. These peaks were assigned to A_g translatory, E_{2g} translatory, and E_{1g} libration modes of $Eu(OH)_3$ NRs, respectively [32]. Enhancement of the Raman peaks intensity was observed for the 1 % Ni–$Eu(OH)_3$ NRs with no significant change in the peak position. However, in the case of 10 % Ni–$Eu(OH)_3$, lower Raman intensity was observed. Moreover, $Eu(OH)_3$ translatory and libration modes of 10 % Ni–$Eu(OH)_3$ NRs have become broader which might be due to the breakdown of the lattice periodicity and long-range translational crystal symmetry caused by the doping of Ni^{2+} into the crystal lattice [33].

3.3. Transmission electron microscopy

TEM analysis of $Eu(OH)_3$, 1 % Ni–$Eu(OH)_3$, and 5 % Ni–$Eu(OH)_3$ was carried out to determine the morphology and size. Fig. 3 shows the TEM images and SAED patterns of $Eu(OH)_3$, 1 % Ni–$Eu(OH)_3$, and 5 % Ni–$Eu(OH)_3$. In general, $Eu(OH)_3$ shows rod-like morphology [7,13,15,25,34,35]. It was observed that the synthesized materials also possess rod-like morphology as can be observed in Fig. 3. Fig. 3(a) shows the TEM image of $Eu(OH)_3$ NRs with an average length of 27 nm and 8 nm in diameter. In general, the growth of particles is influenced by initial pH, reaction time, and temperature [36]. In this case, the initial pH, temperature, and reaction time were all consistent. Therefore, the difference in the particle size mainly depends on the addition of Ni^{2+} ions. When 1 % Ni was incorporated into $Eu(OH)_3$, the TEM image of 1 % Ni–$Eu(OH)_3$ shows nanorods with an average length of 34 nm and diameter of 10 nm as shown in Fig. 3(c). It was observed that the particle size has slightly increased with Ni^{2+} doping. The particle size was observed to be similar to 1 % Ni–$Eu(OH)_3$ when 5 % Ni was incorporated. The 5 % Ni–$Eu(OH)_3$ NRs showed an average length of 33 nm and diameter of 9 nm (Fig. 3(e)). This suggests that 5 % Ni doping has no significant influence on the particle size of $Eu(OH)_3$. However, when 10 % Ni was incorporated, the particle length was increased to 50 nm and the diameter was increased to 13 nm (Fig. 3(g)). This shows that a further increase in the percentage doping of Ni^{2+} significantly influenced the particle size of $Eu(OH)_3$. The increase of the particle size might be due to the kinetics of the formation reaction of $Eu(OH)_3$ and Ni–$Eu(OH)_3$, the different particle

Table 1
Average crystallite size (nm), lattice parameters (Å), cell volume (Å^3), and average lattice strain (ε) of $Eu(OH)_3$, and Ni–$Eu(OH)_3$ NRs.

Samples	Average crystallite size (nm)	Lattice parameter (Å)		Cell volume (Å^3)	Average lattice strain (ε)
		a	c		
$Eu(OH)_3$	35.84	6.36	4.19	146.8	0.0018
1 % Ni–$Eu(OH)_3$	22.09	6.34	4.22	146.9	0.0021
5 % Ni–$Eu(OH)_3$	21.88	6.36	4.22	147.8	0.0018
10 % Ni–$Eu(OH)_3$	24.14	6.34	4.20	146.2	0.0015

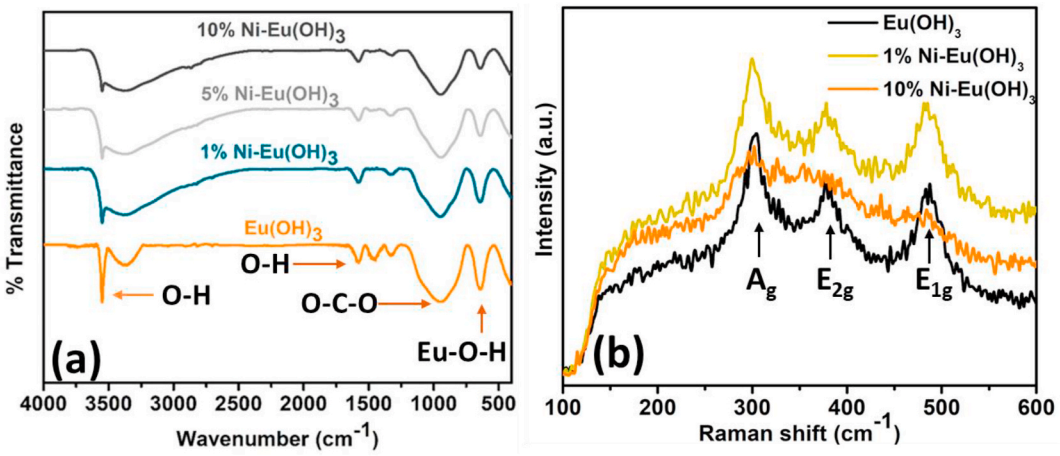

Fig. 2. **(a)** FT-IR of $Eu(OH)_3$, 1, 5, and 10 % Ni–$Eu(OH)_3$ NRs, and **(b)** Raman spectra of $Eu(OH)_3$, 1, and 10 % Ni–$Eu(OH)_3$ NRs.

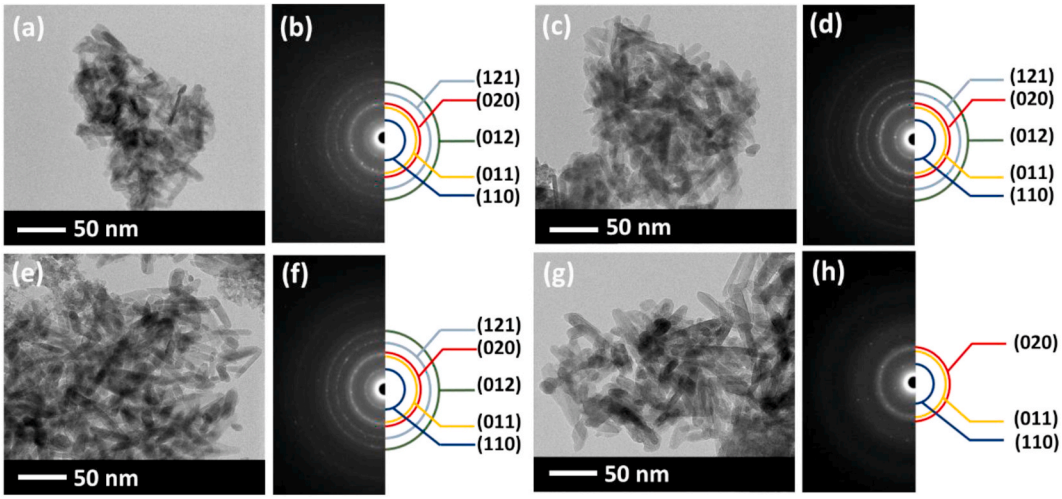

Fig. 3. TEM images and SAED patterns of **(a)–(b)** $Eu(OH)_3$, **(c)–(d)** 1 % Ni–$Eu(OH)_3$, **(e)–(f)** 5 % Ni–$Eu(OH)_3$, and **(g)–(h)** 10 % Ni–$Eu(OH)_3$, respectively.

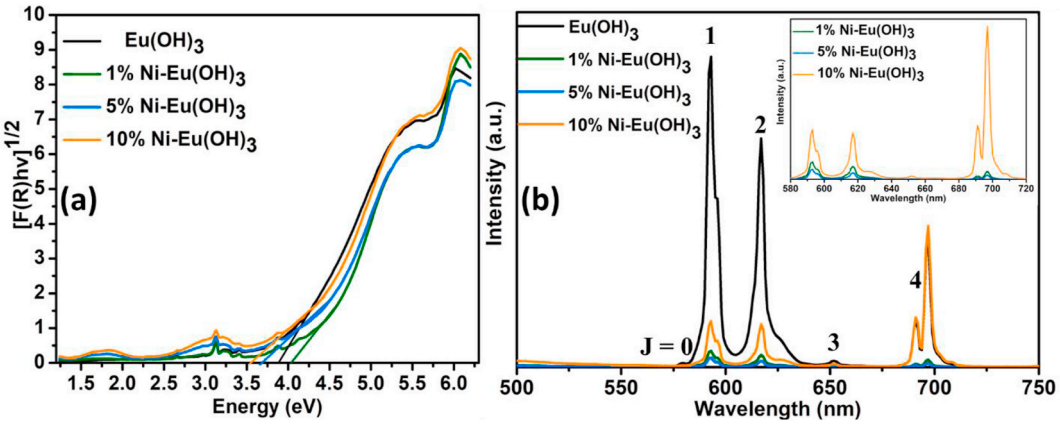

Fig. 4. **(a)** Tauc plot obtained from Kubelka-Munk function for band gap energy estimation and **(b)** PL spectra of $Eu(OH)_3$ and 1, 5, and 10 % Ni–Eu$(OH)_3$ NPs (**inset**: zoomed PL of Ni–$Eu(OH)_3$).

growth rate or the presence of structural disorder and strain in the lattice due to different ionic radii [37].

Moreover, to evaluate the phase and crystallinity of $Eu(OH)_3$, 1 % Ni–$Eu(OH)_3$, and 5 % Ni–$Eu(OH)_3$ NRs, SAED was used and shown in Fig. 3(b), (d), and **(f)**. Five broad rings were observed for $Eu(OH)_3$, 1 % Ni–$Eu(OH)_3$, and 5 % Ni–$Eu(OH)_3$ NRs which are attributed to the (110), (011), (020), (121), and (012) reflections of the hexagonal $Eu(OH)_3$ ($P6_3/m$) structure. Fig. 3(h) shows three rings of 10 % Ni–$Eu(OH)_3$ which are attributed to (110), (011), and (020). Original SAED images can be observed in Fig. S1. This is in agreement with the XRD results as discussed in Section 3.1. This further confirms the successful synthesis of $Eu(OH)_3$ and doping of Ni^{2+} in the $Eu(OH)_3$.

3.4. UV–Vis diffuse reflectance spectroscopy and photoluminescence spectroscopy

UV–Vis DRS analysis was used to estimate the band gap energies of $Eu(OH)_3$, 1, 5, and 10 % Ni–$Eu(OH)_3$ NRs. Fig. 4(a) depicts the Tauc plot obtained from the Kubelka-Munk function using the following equation (**Eq. 4**):

$$F(R) = \left(\frac{(1-R)^2}{2R} \times h\nu \right)^{\frac{1}{2}} \tag{4}$$

where R is the measured absolute reflectance of the samples. The band gap energy of $Eu(OH)_3$ and Ni–$Eu(OH)_3$ NRs was obtained from the plots of $[F(R)h\nu]^{1/2}$ versus $h\nu$ and shown in Table 2.

The effect of doping on the band gap energy was observed. $Eu(OH)_3$ showed a band gap energy of 3.80 eV which is in good agreement with the literature [13]. The band gap energy was increased slightly to 4.06 eV after doping with 1 % Ni. This might be due to the high crystallinity of the 1 % Ni–$Eu(OH)_3$ as can be observed from the XRD analysis. High crystallinity can be associated with fewer defects and less disorder which can lead to a wide band gap energy [38]. However, the band gap energy was decreased to 3.69 eV as expected when 5 % Ni was doped into $Eu(OH)_3$. Similarly, a further increase in doping concentration would result in the decrease of the band gap energy as observed in the case of 10 % Ni–$Eu(OH)_3$ which showed about 3.50 eV. The band gap energies of $Eu(OH)_3$ and Ni–$Eu(OH)_3$ NRs are tabulated in Table 2.

In addition to the UV–Vis DRS, PL analysis of $Eu(OH)_3$ and Ni–$Eu(OH)_3$ NRs was carried out to understand the optical behavior of the samples. Fig. 4(b) exhibits the PL emission spectra of $Eu(OH)_3$, 1 % Ni–$Eu(OH)_3$, 5 % Ni–$Eu(OH)_3$, and, 10 % Ni–$Eu(OH)_3$ NRs at an excitation wavelength of 321 nm in which the emission peaks were observed in the range of 500 – 750 nm. The PL peaks were associated with the $^5D_0 \rightarrow {}^7F_J$ (J = 0–4) transitions. $Eu(OH)_3$ NRs showed PL peaks at approximately ~ 578, 592, 617, 651, and 690 nm which correspond to $^5D_0 \rightarrow {}^7F_0$, $^5D_0 \rightarrow {}^7F_1$, $^5D_0 \rightarrow {}^7F_2$, $^5D_0 \rightarrow {}^7F_3$, and $^5D_0 \rightarrow {}^7F_4$ transitions, respectively [15]. However, the PL peaks were quenched greatly when 1 % Ni was doped into $Eu(OH)_3$. The PL intensity was further decreased for 5 % Ni–$Eu(OH)_3$ NRs. On the other hand, 10 % Ni–$Eu(OH)_3$ showed an enhanced PL intensity which was higher than both 1 % Ni–$Eu(OH)_3$ NRs and 5 % Ni–$Eu(OH)_3$ NRs. It is stated that high recombination of charge carriers would result in high PL intensity [39]. Therefore, in this case, pure $Eu(OH)_3$ showed the highest PL intensity while Ni–$Eu(OH)_3$ showed lower intensity suggesting low recombination of charge carriers. Amongst Ni–$Eu(OH)_3$ NRs, it was observed that 10 % Ni–$Eu(OH)_3$ might show more recombination of photogenerated electron-hole pair than 1 and 5 % Ni–$Eu(OH)_3$ NRs. Table 2 shows the wavelength of each PL peak of $Eu(OH)_3$ and Ni–$Eu(OH)_3$ NRs. It was observed that the PL peaks corresponding to $^5D_0 \rightarrow {}^7F_0$ and $^5D_0 \rightarrow {}^7F_3$ were flattened. This might be due to the forbidden transition for $^5D_0 \rightarrow {}^7F_0$ and $^5D_0 \rightarrow {}^7F_3$ both in magnetic and electric dipole schemes [40].

3.5. X-ray photoelectron spectroscopy

X-ray photoelectron spectroscopy (XPS) was performed at room temperature to investigate the chemical state and the electronic structure of the elements in $Eu(OH)_3$, 1 % Ni–$Eu(OH)_3$, 5 % Ni–$Eu(OH)_3$ and 10 % Ni–$Eu(OH)_3$ (Fig. 5). Fig. 5(a) shows the complete survey scan spectra of the samples, which confirmed the presence of Ni 2*p*, O 1*s*, and Eu 4*d*. The Eu 4*d* core level peak is shown in Fig. 5 (b). Eu^{3+} $4d_{3/2}$ and Eu^{3+} $4d_{5/2}$ were found at 141.9 and 136.2 eV, respectively [41]. A slight shift was observed in the binding energy of Eu^{3+} $4d_{3/2}$ and Eu^{3+} $4d_{5/2}$ when doped with Ni^{2+}. The binding energy was shifted to higher energy when doped with more Ni^{2+} ions.

Fig. 5(c) shows the XPS spectrum of O 1*s* where all samples showed one major peak at approximately 528 eV. This indicates the presence of nucleophilic oxygen species which is OH^- anion, in $Eu(OH)_3$ and Ni–$Eu(OH)_3$ NRs [42]. The XPS peak intensity decreased slightly from $Eu(OH)_3$–10 % Ni–$Eu(OH)_3$ NRs. However, no significant change in the peak position was observed for all the samples. Ni 2*p* spectra of Ni–$Eu(OH)_3$ NRs can be observed in Fig. 5(d). Two prominent peaks can only be observed for 10 % Ni–$Eu(OH)_3$ at 854.26

Table 2
Calculated band gap energies and PL wavelength of $Eu(OH)_3$ and Ni–$Eu(OH)_3$ NRs.

Sample	UV–Vis DRS	PL wavelength (nm)				
	Band gap energy (eV)	$^5D_0 \rightarrow {}^7F_0$	$^5D_0 \rightarrow {}^7F_1$	$^5D_0 \rightarrow {}^7F_2$	$^5D_0 \rightarrow {}^7F_3$	$^5D_0 \rightarrow {}^7F_4$
$Eu(OH)_3$	3.80	578	592	617	651	691 and 697
1 % Ni–$Eu(OH)_3$	4.06	–	592	616	–	691 and 697
5 % Ni–$Eu(OH)_3$	3.69	–	592	616	–	690 and 697
10 % Ni–$Eu(OH)_3$	3.50	–	593	616	651	690 and 697

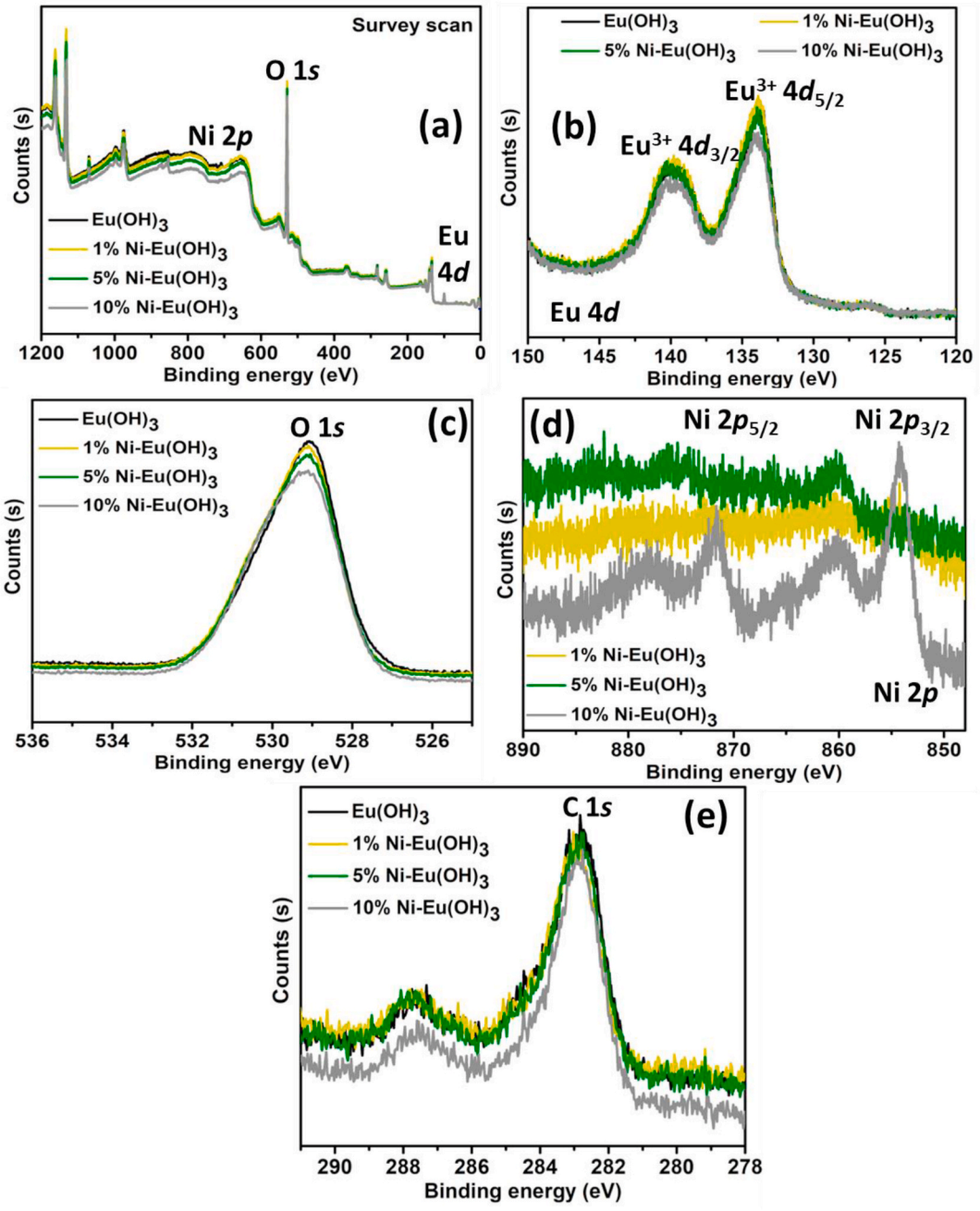

Fig. 5. XPS: **(a)** Survey scan, **(b)** Eu 4*d*, **(c)** O 1*s*, **(d)** Ni 2*p*, and **(e)** C 1*s* of $Eu(OH)_3$ and Ni–$Eu(OH)_3$ NRs.

Table 3
The atomic concentration of C 1*s*, O 1*s*, Eu 4*d*, and Ni 2*p* of $Eu(OH)_3$, 1 % Ni–$Eu(OH)_3$. 5 % Ni–$Eu(OH)_3$, and 10 % Ni–$Eu(OH)_3$ NRs.

Samples	Atomic concentrations (%)			
	C 1*s*	O 1*s*	Eu 4*d*	Ni 2*p*
$Eu(OH)_3$	11.5	58.9	29.6	–
1 % Ni–$Eu(OH)_3$	5.4	58.5	30.7	5.4
5 % Ni–$Eu(OH)_3$	4.7	57.6	28.7	9.0
10 % Ni–$Eu(OH)_3$	5.3	55.7	25.4	13.6

eV and 871.50 eV, which corresponds to Ni $2p_{3/2}$ and Ni $2p_{1/2}$, respectively [43]. The XPS spectra of 1 % and 5 % Ni–$Eu(OH)_3$ NRs showed weak signals which might be due to the small content of Ni in the samples [43]. Satellite peaks at 860.22 eV and 877.83 eV suggest the presence of Ni^{2+} ions in the $Eu(OH)_3$ lattice [44,45]. The typical C 1*s* were observed at about 282 eV in the spectra (Fig. 5 (e)). The atomic concentrations of C 1*s*, O 1*s*, Eu 4*d*, and Ni 2*p* are listed in Table 3.

4. Applications

4.1. Photocatalytic degradation of 4-nitrophenol

The colourless organic pollutant i.e., 4-NP was photocatalytically degraded under UV light irradiation using $Eu(OH)_3$ and Ni–Eu $(OH)_3$ NRs. The experiment was carried out for 5 h and the absorbance of the reaction solution was measured at every hour to observe the progress of the photocatalytic activities of $Eu(OH)_3$ and Ni–$Eu(OH)_3$ NRs. The experiment was conducted in triplicates to ensure the repeatability of the results and avoid any errors. Fig. 6(a) shows the average percentage and ln C_0/C of the photocatalytic degradation of 4-NP using $Eu(OH)_3$ and Ni–$Eu(OH)_3$ NRs, respectively.

Fig. 6(a) at 0 h, shows the adsorption-desorption phase (in the dark), in which $Eu(OH)_3$ and 5 % Ni–$Eu(OH)_3$ NRs have low adsorption affinity towards 4-NP which are about 28.45 ± 3.88 % and 28.49 ± 4.07 % respectively, while 10 % Ni–$Eu(OH)_3$ has the highest adsorption affinity (33.69 ± 3.98 %). When illuminated with UV light, the percentage degradation of 4-NP gradually increased with time. After 5 h of UV irradiation, 10 % Ni–$Eu(OH)_3$ NRs showed the highest photocatalytic activity with a total of 74.29 ± 7.53 % as shown in Fig. 6(a) and Table 4. The effectiveness of the photocatalytic degradation of 4-NP was observed as follows: 10 % Ni–Eu $(OH)_3$ > 5 % Ni–$Eu(OH)_3$ > 1 % Ni–$Eu(OH)_3$ > $Eu(OH)_3$. The photocatalytic degradation activity was observed to be enhanced with increasing the percentage of Ni doping. The efficiency of 10 % Ni–$Eu(OH)_3$ NRs might be due to its band gap energy which is about 3.50 eV. Moreover, 5 % Ni–$Eu(OH)_3$ also showed slightly higher band gap energy which is about 3.69 eV suggesting a similar response in the photocatalytic activity. One should note that even though the PL intensity of 5 % Ni–$Eu(OH)_3$ (Fig. 4(b): inset) exhibits the lowest intensity, which in general indicates the maximum separation of charge carriers that is very useful for efficient photocatalytic

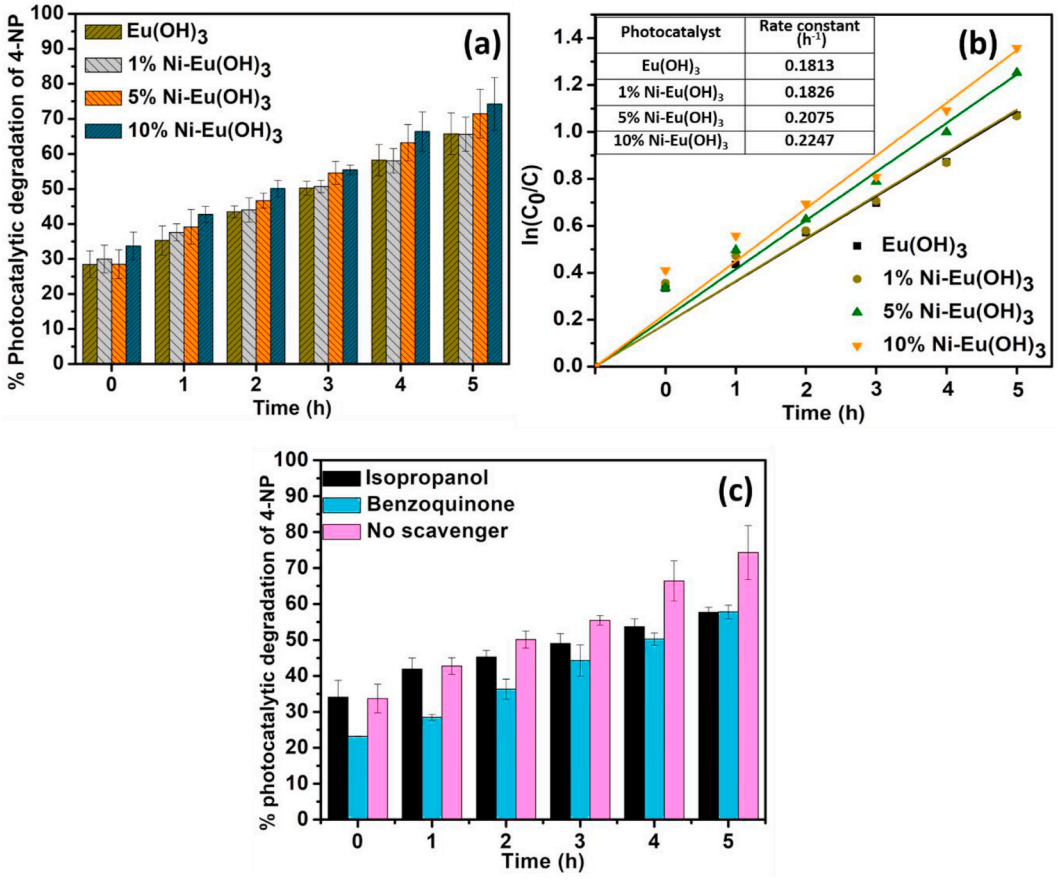

Fig. 6. The average of **(a)** percentage, **(b)** ln C_0/C plot against time for the photocatalytic degradation of 4-NP using $Eu(OH)_3$, 1 % Ni–$Eu(OH)_3$, 5 % Ni–$Eu(OH)_3$, and 10 % Ni–$Eu(OH)_3$, and **(c)** average percentage photocatalytic degradation of 4-NP for trapping experiment of 10 % Ni–$Eu(OH)_3$ under UV light irradiation.

Table 4
The average percentage photocatalytic activities of $Eu(OH)_3$ and 1, 5, and 10 % Ni–$Eu(OH)_3$ NRs for 4-NP degradation under UV light irradiation.

	% Photocatalytic degradation of 4-NP					
	Ads-des	1 h	2 h	3 h	4 h	5 h
$Eu(OH)_3$	28.45 ± 3.88	35.27 ± 4.18	43.47 ± 1.68	50.20 ± 1.94	58.19 ± 4.46	65.75 ± 5.97
1 % Ni–$Eu(OH)_3$	29.98 ± 3.96	37.58 ± 2.46	43.98 ± 3.47	50.69 ± 1.74	58.03 ± 3.50	65.63 ± 4.89
5 % Ni–$Eu(OH)_3$	28.49 ± 4.07	39.17 ± 4.95	46.64 ± 2.13	54.58 ± 3.24	63.19 ± 5.19	71.43 ± 6.96
10 % Ni–$Eu(OH)_3$	33.69 ± 3.98	42.72 ± 2.31	50.10 ± 2.37	55.45 ± 1.37	66.42 ± 5.58	74.29 ± 7.53

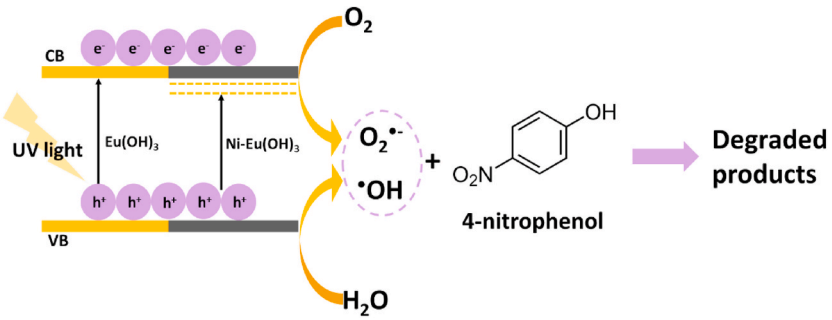

Fig. 7. The proposed mechanism for the photocatalytic degradation of 4-NP using $Eu(OH)_3$ and Ni–$Eu(OH)_3$ NRs under UV light irradiation.

performance, the 10 % Ni–$Eu(OH)_3$ showed the narrowest band gap energy which facilitated the UV light adsorption. The doping might help in creating defect states in the band gap which enables UV light absorption and thus inhibits rapid charge carrier recombination [46]. Moreover, at adsorption and desorption, it was found that 10 % Ni–$Eu(OH)_3$ showed the highest response which might facilitate the overall photocatalytic response [47]. Therefore, 10 % Ni–$Eu(OH)_3$ showed the best photocatalytic activity. On the other hand, both $Eu(OH)_3$ and 1 % Ni–$Eu(OH)_3$ also showed similar photocatalytic responses due to their band gap energies i.e., 3.80 and 4.06 eV, respectively.

Moreover, the photocatalytic activity of $Eu(OH)_3$ and Ni–$Eu(OH)_3$ NRs against 4-NP was studied by applying the pseudo-first-order kinetics as shown below (**Eq. (5)**):

$$ln\frac{C_0}{C} = Kt \tag{5}$$

C_0 and C denote the original and the treated concentration of 4-NP while t is the photocatalytic reaction time in h. The rate constant of the pseudo-first-order (K) is expressed in h^{-1}. Fig. 6(b) presents the pseudo-first-order kinetics of the photocatalytic degradation of 4-NP activity. The rate constants of $Eu(OH)_3$, 1 % Ni–$Eu(OH)_3$, 5 % Ni–$Eu(OH)_3$, and 10 % Ni–$Eu(OH)_3$ NRs were estimated to be 0.1813, 0.1826, 0.2075, and 0.2247 h^{-1}, respectively. It was observed that the rate constant was increased with more Ni-doping. This suggests that the doping of Ni^{2+} into $Eu(OH)_3$ has improved the photocatalytic degradation of 4-NP. Moreover, radicals trapping experiments were conducted for 10 % Ni–$Eu(OH)_3$ with the addition of isopropanol and benzoquinone separately. As can be seen in Fig. 6(c), the photocatalytic degradation of 4-NP with the addition of benzoquinone showed a reduction in the photocatalytic response from the beginning of the experiment as compared to the photocatalytic reaction without scavengers. Benzoquinone is responsible for scavenging $O_2^{\bullet-}$ radicals. Isopropanol which is responsible for the scavenger of •OH radicals also showed a reduction in the photocatalytic degradation activity although not as much as benzoquinone. Despite that, at 5 h, photocatalytic degradation of 4-NP with isopropanol showed a similar response as benzoquinone.

In the photocatalytic degradation of 4-NP, •OH radicals are reported to play an important role [48,49]. Moreover, $O_2^{\bullet-}$ is also involved in the photocatalytic degradation reaction as suggested by Kang et al. [50]. Based on the radical trapping experiment (Fig. 6 (c)), both •OH and $O_2^{\bullet-}$ radicals were trapped which showed a reduction in the performance of photocatalytic degradation of 4-NP. Therefore, the involvement of •OH and $O_2^{\bullet-}$ radicals improved the overall photocatalytic activity. Fig. 7 illustrates the general mechanism of the photocatalytic degradation of 4-NP.

5. Conclusions

The synthesis of $Eu(OH)_3$ and Ni–$Eu(OH)_3$ NRs was carried out using a microwave-assisted synthesis method. The properties of the synthesized materials such as their structural, optical, morphological properties, and photocatalytic activities were investigated. All the synthesized materials i.e., $Eu(OH)_3$ and 1, 5, and 10 % Ni–$Eu(OH)_3$ have acquired hexagonal phases based on the XRD studies. FT-IR and Raman studies confirmed the synthesis of $Eu(OH)_3$ and Ni–$Eu(OH)_3$. All the materials showed rod-like morphology with average length and diameter between 27 – 50 nm and 8–13 nm, respectively. The band gap energies of $Eu(OH)_3$ and Ni–$Eu(OH)_3$ were

decreased with an increase in Ni-doping. Owing to that, the PL study showed a decrease in PL intensity for Ni–$Eu(OH)_3$ NRs. The photocatalytic degradation of 4-NP activity was conducted and it showed that 10 % Ni–$Eu(OH)_3$ NRs exhibited enhanced photocatalytic activity under UV light irradiation. The kinetic study was also carried out using the pseudo-first-order kinetics in which 10 % Ni–$Eu(OH)_3$ showed a rate constant of 0.2247 h^{-1}. Therefore, Ni–$Eu(OH)_3$ has potential to be a UV light-responsive material for the photocatalytic degradation of colourless pollutants.

Data availability

Data will be supplied upon request.

CRediT authorship contribution statement

Shaidatul Najihah Matussin: Writing – original draft, Methodology, Investigation, Data curation. **Fazlurrahman Khan:** Formal analysis, Data curation. **Mohammad Hilni Harunsani:** Writing – original draft, Supervision. **Young-Mog Kim:** Resources, Formal analysis. **Mohammad Mansoob Khan:** Writing – review & editing, Supervision, Funding acquisition, Conceptualization.

Declaration of competing interest

The authors declare that they have no known competing financial interests or personal relationships that could have appeared to influence the work reported in this paper.

Acknowledgement

The authors would like to acknowledge the FRC grants (UBD/RSCH/1.4/FICBF(b)/2022/046 and UBD/RSCH/1.4/FICBF(b)/2023/059) received from Universiti Brunei Darussalam, Brunei Darussalam. This research was supported by the Basic Science Research Program through the National Research Foundation (NRF) of Korea grant funded by the Ministry of Education (2021R1A6A1A03039211, 2022R1A2B5B01001998, and RS-2023-00241461).

Appendix A. Supplementary data

Supplementary data to this article can be found online at https://doi.org/10.1016/j.heliyon.2024.e32719.

References

[1] S.N. Matussin, M.H. Harunsani, M.M. Khan, CeO2 and CeO2-based nanomaterials for photocatalytic, antioxidant and antimicrobial activities, J. Rare Earths 41 (2023) 167–181, https://doi.org/10.1016/j.jre.2022.09.003.
[2] S.N. Matussin, F. Khan, M.H. Harunsani, Y.-M. Kim, M.M. Khan, Visible-light-induced photocatalytic and photoantibacterial activities of Co-doped CeO_2, ACS Omega 8 (2023) 11868–11879, https://doi.org/10.1021/acsomega.2c07058.
[3] S.N. Matussin, F. Khan, M.H. Harunsani, Y.-M. Kim, M.M. Khan, Effect of Pd-doping concentrations on the photocatalytic, photoelectrochemical, and photoantibacterial properties of CeO2, Catalysts 13 (2023) 96, https://doi.org/10.3390/catal13010096.
[4] S. Seal, A. Jeyaranjan, C.J. Neal, U. Kumar, T.S. Sakthivel, D.C. Sayle, Engineered defects in cerium oxides: tuning chemical reactivity for biomedical, environmental, & energy applications, Nanoscale 12 (2020) 6879–6899, https://doi.org/10.1039/D0NR01203C.
[5] M.M. Khan, S.N. Matussin, Sm_2O_3 and Sm_2O_3 -based nanostructures for photocatalysis, sensors, CO conversion, and biological applications, Catal. Sci. Technol. 13 (2023) 2274–2290, https://doi.org/10.1039/D2CY01976K.
[6] D.D. Dionysiou, S. Rtimi, E. Kowalska, C. Han, M. Janczarek, Novel photocatalysts for environmental and energy applications, Catalysts 12 (2022) 458, https://doi.org/10.3390/catal12050458.
[7] X. Ji, P. Hu, X. Li, L. Zhang, J. Sun, Hydrothermal control, characterization, growth mechanism, and photoluminescence properties of highly crystalline 1D Eu(OH)3nanostructures, RSC Adv. 10 (2020) 33499–33508, https://doi.org/10.1039/d0ra04338a.
[8] M.M. Khan, Theoretical Concepts of Photocatalysis, Elsevier, 2023, https://doi.org/10.1016/C2021-0-01798-3.
[9] K.O. Abdulwahab, M.M. Khan, J.R. Jennings, Doped ceria nanomaterials: preparation, properties, and uses, ACS Omega 8 (2023) 30802–30823, https://doi.org/10.1021/acsomega.3c01199.
[10] S.N. Matussin, F. Khan, M.H. Harunsani, Y.-M. Kim, M.M. Khan, Impact of Co-doping on the visible light-driven photocatalytic and 2 photoelectrochemical activities of Eu(OH)3, ACS Omega 9 (14) (2024) 16420–16428. https://doi.org/10.1021/acsomega.3c10416.
[11] S.N. Matussin, F. Khan, P. Chandika, M.H. Harunsani, N. Ahmad, Y.-M. Kim, W.-K. Jung, M.M. Khan, α-Glucosidase inhibitory activity and cytotoxicity of CeO_2 nanoparticles fabricated using a mixture of different cerium precursors, ACS Omega 9 (2024) 157–165, https://doi.org/10.1021/acsomega.3c02524.
[12] I. Khan, K. Saeed, I. Khan, Nanoparticles: properties, applications and toxicities, Arab. J. Chem. 12 (2019) 908–931, https://doi.org/10.1016/j.arabjc.2017.05.011.
[13] S. Liu, Y. Cai, X. Cai, H. Li, F. Zhang, Q. Mu, Y. Liu, Y. Wang, Catalytic photodegradation of Congo red in aqueous solution by Ln(OH) 3 (Ln = Nd, Sm, Eu, Gd, Tb, and Dy) nanorods, Appl. Catal. Gen. 453 (2013) 45–53, https://doi.org/10.1016/j.apcata.2012.12.004.
[14] S.N. Matussin, M.H. Harunsani, M.M. Khan, Eu(OH)3 and Eu(OH)3-based nanostructures: synthesis, properties, and uses, Mater. Today Commun. 39 (2024) 108775, https://doi.org/10.1016/j.mtcomm.2024.108775.
[15] Q.G. Zeng, Z.J. Ding, Z.M. Zhang, Y.Q. Sheng, Photoluminescence and Raman spectroscopy studies of Eu(OH)3 rods at high pressures, J. Phys. Chem. C 114 (2010) 4895–4900, https://doi.org/10.1021/jp911791u.
[16] C.R. Patra, S.S. Abdel Moneim, E. Wang, S. Dutta, S. Patra, M. Eshed, P. Mukherjee, A. Gedanken, V.H. Shah, D. Mukhopadhyay, In vivo toxicity studies of europium hydroxide nanorods in mice, Toxicol. Appl. Pharmacol. 240 (2009) 88–98, https://doi.org/10.1016/j.taap.2009.07.009.

[17] L. Zhang, W. Hu, Y. Wu, P. Wei, L. Dong, Z. Hao, S. Fan, Y. Song, Y. Lu, C. Liang, L. Wen, Microwave-assisted facile synthesis of Eu(OH)3 nanoclusters with pro-proliferative activity mediated by miR-199a-3p, ACS Appl. Mater. Interfaces 10 (2018) 31044–31053, https://doi.org/10.1021/acsami.8b10543.

[18] S. Laha, K.P. Petrova, Biodegradation of 4-nitrophenol by indigenous microbial population in Everglades soils, Biodegradation 8 (1997) 349–356, https://doi.org/10.1023/A:1008285717595.

[19] A. Verma, D.P. Jaihindh, Y.P. Fu, Photocatalytic 4-nitrophenol degradation and oxygen evolution reaction in CuO/g-C3N4 composites prepared by deep eutectic solvent-assisted chlorine doping, Dalton Trans. 48 (2019) 8594–8610, https://doi.org/10.1039/c9dt01046g.

[20] Y. Fan, D. Wu, S. Zhang, L. Zhang, W. Hu, C. Zhu, X. Gong, Effective photodegradation of 4-nitrophenol with CuO nano particles prepared by ionic liquids/water system, Green Chemical Engineering 3 (2022) 15–24, https://doi.org/10.1016/j.gce.2021.07.009.

[21] O.A. Osin, T. Yu, X. Cai, Y. Jiang, G. Peng, X. Cheng, R. Li, Y. Qin, S. Lin, Photocatalytic degradation of 4-nitrophenol by C, N-TiO2: degradation efficiency vs. embryonic toxicity of the resulting compounds, Front. Chem. 6 (2018), https://doi.org/10.3389/fchem.2018.00192.

[22] S.N. Matussin, F. Khan, M.H. Harunsani, Y.-M. Kim, M.M. Khan, Photocatalytic degradation of brilliant green and 4-nitrophenol using Ni-doped Gd(OH)3 nanorods, Sci. Rep. 14 (2024) 8269, https://doi.org/10.1038/s41598-024-58688-2.

[23] MdR. Al-Mamun, MdZ. Iqbal Rokon, MdA. Rahim, MdI. Hossain, MdS. Islam, MdR. Ali, M.S. Bacchu, H. Waizumi, T. Komeda, M.Z. Hossain Khan, Enhanced photocatalytic activity of Cu and Ni-doped ZnO nanostructures: a comparative study of methyl orange dye degradation in aqueous solution, Heliyon 9 (2023) e16506, https://doi.org/10.1016/j.heliyon.2023.e16506.

[24] S.N. Matussin, F. Khan, M.H. Harunsani, Y.-M. Kim, M.M. Khan, Impact of Co-doping on the visible light-driven photocatalytic and photoelectrochemical activities of $Eu(OH)_3$, ACS Omega 9 (2024) 16420–16428, https://doi.org/10.1021/acsomega.3c10416.

[25] J.G. Kang, Y. Jung, B.K. Min, Y. Sohn, Full characterization of Eu(OH) 3 and Eu 2 O 3 nanorods, Appl. Surf. Sci. 314 (2014) 158–165, https://doi.org/10.1016/j.apsusc.2014.06.165.

[26] D. Lee, J. Seo, L.D.L.S. Valladares, O. Avalos Quispe, C.H.W. Barnes, Magnetic and structural properties of yellow europium oxide compound and Eu(OH)3, J. Solid State Chem. 228 (2015) 141–145, https://doi.org/10.1016/j.jssc.2015.04.018.

[27] D.F. Mullica, W.O. Milligan, G.W. Beall~, CRYSTAL STRUCTURES OF Pr(OH)3, Eu(OH)3 AND Tm(OHh t, 1979.

[28] J.S. Revathy, N.S.C. Priya, K. Sandhya, D.N. Rajendran, Structural and optical studies of cerium doped gadolinium oxide phosphor, Bull. Mater. Sci. 44 (2021) 13, https://doi.org/10.1007/s12034-020-02299-w.

[29] R. Sagheer, M. Khalil, V. Abbas, Z.N. Kayani, U. Tariq, F. Ashraf, Effect of Mg doping on structural, morphological, optical and thermal properties of ZnO nanoparticles, Optik 200 (2020), https://doi.org/10.1016/j.ijleo.2019.163428.

[30] S.N. Matussin, M.H. Harunsani, A.L. Tan, M.H. Cho, M.M. Khan, Effect of Co2+ and Ni2+ co-doping on SnO2 synthesized via phytogenic method for photoantioxidant studies and photoconversion of 4-nitrophenol, Mater. Today Commun. 25 (2020) 101677, https://doi.org/10.1016/j.mtcomm.2020.101677.

[31] S.N. Matussin, A.L. Tan, M.H. Harunsani, M.H. Cho, M.M. Khan, Green and phytogenic fabrication of Co-doped SnO2 using aqueous leaf extract of tradescantia spathacea for photoantioxidant and photocatalytic studies, Bionanoscience 11 (2021) 120–135, https://doi.org/10.1007/s12668-020-00820-3.

[32] Q. Mu, Y. Wang, A simple method to prepare Ln(OH)3 (Ln = La, Sm, Tb, Eu, and Gd) nanorods using CTAB micelle solution and their room temperature photoluminescence properties, J. Alloys Compd. 509 (2011) 2060–2065, https://doi.org/10.1016/j.jallcom.2010.10.141.

[33] D. Komaraiah, E. Radha, J. James, N. Kalarikkal, J. Sivakumar, M.V. Ramana Reddy, R. Sayanna, Effect of particle size and dopant concentration on the Raman and the photoluminescence spectra of TiO 2 :Eu 3+ nanophosphor thin films, J. Lumin. 211 (2019) 320–333, https://doi.org/10.1016/j.jlumin.2019.03.050.

[34] P.F. Wei, L. Zhang, S.K. Nethi, A.K. Barui, J. Lin, W. Zhou, Y. Shen, N. Man, Y.J. Zhang, J. Xu, C.R. Patra, L.P. Wen, Accelerating the clearance of mutant huntingtin protein aggregates through autophagy induction by europium hydroxide nanorods, Biomaterials 35 (2014) 899–907, https://doi.org/10.1016/j.biomaterials.2013.10.024.

[35] C. Tian, L. Wang, F. Luan, X. Fu, X. Zhuang, L. Chen, A novel electrochemiluminescent emitter of europium hydroxide nanorods and its application in bioanalysis, Chem. Commun. 55 (2019) 12479–12482, https://doi.org/10.1039/c9cc07129f.

[36] A.K. Parchur, R.S. Ningthoujam, Preparation and structure refinement of Eu3+ doped CaMoO4 nanoparticles, Dalton Trans. 40 (2011) 7590, https://doi.org/10.1039/c1dt10327j.

[37] T. Dippong, O. Cadar, E.A. Levei, Effect of transition metal doping on the structural, morphological, and magnetic properties of NiFe2O4, Materials 15 (2022) 2996, https://doi.org/10.3390/ma15092996.

[38] E. Laghchim, A. Raidou, A. Fahmi, E. Ouabida, M. Fahoume, Exploring the correlation between the bandgap engineering and defect density toward high CTS solar cell efficiency, Mater. Today Commun. 37 (2023) 106949, https://doi.org/10.1016/j.mtcomm.2023.106949.

[39] A.N. Kadam, J. Lee, S.V. Nipane, S.-W. Lee, Nanocomposites for visible light photocatalysis, in: Nanostructured Materials for Visible Light Photocatalysis, Elsevier, 2022, pp. 295–317, https://doi.org/10.1016/B978-0-12-823018-3.00017-8.

[40] D. Wang, C. Zheng, L. Fan, Y. Hu, J. Zheng, Photoluminescence behavior of europium (III) complexes containing 1-(4-tert-butylphenyl)-3-(2-naphthyl)-propane-1,3-dione ligand, Spectrochim. Acta Mol. Biomol. Spectrosc. 117 (2014) 245–249, https://doi.org/10.1016/j.saa.2013.08.023.

[41] D. Zhang, X. He, H. Yang, L. Shi, J. Fang, Surfactant-assisted reflux synthesis, characterization and formation mechanism of carbon nanotube/europium hydroxide core-shell nanowires, Appl. Surf. Sci. 255 (2009) 8270–8275, https://doi.org/10.1016/j.apsusc.2009.05.099.

[42] T.E. Jones, T.C.R. Rocha, A. Knop-Gericke, C. Stampfl, R. Schlögl, S. Piccinin, Thermodynamic and spectroscopic properties of oxygen on silver under an oxygen atmosphere, Phys. Chem. Chem. Phys. 17 (2015) 9288–9312, https://doi.org/10.1039/C5CP00342C.

[43] S.N. Matussin, A.L. Tan, M.H. Harunsani, A. Mohammad, M.H. Cho, M.M. Khan, Effect of Ni-doping on the properties of the SnO2 synthesized using Tradescantia spathacea for photoantioxidant studies, Mater. Chem. Phys. (2020) 123293, https://doi.org/10.1016/j.matchemphys.2020.123293.

[44] A. Yildiz, B. Kayhan, B. Yurduguzel, A.P. Rambu, F. Iacomi, S. Simon, Ni doping effect on electrical conductivity of ZnO nanocrystalline thin films, J. Mater. Sci. Mater. Electron. 22 (2011) 1473–1478, https://doi.org/10.1007/s10854-011-0332-y.

[45] S. Ramya, G. Viruthagiri, R. Gobi, N. Shanmugam, N. Kannadasan, Synthesis and characterization of Ni2+ ions incorporated CuO nanoparticles and its application in antibacterial activity, J. Mater. Sci. Mater. Electron. 27 (2016) 2701–2711, https://doi.org/10.1007/s10854-015-4080-2.

[46] M.R.D. Khaki, M.S. Shafeeyan, A.A.A. Raman, W.M.A.W. Daud, Application of doped photocatalysts for organic pollutant degradation - a review, J. Environ. Manag. 198 (2017) 78–94, https://doi.org/10.1016/j.jenvman.2017.04.099.

[47] T. Wang, P.D. Dissanayake, M. Sun, Z. Tao, W. Han, N. An, Q. Gu, D. Xia, B. Tian, Y.S. Ok, J. Shang, Adsorption and visible-light photocatalytic degradation of organic pollutants by functionalized biochar: role of iodine doping and reactive species, Environ. Res. 197 (2021) 111026, https://doi.org/10.1016/j.envres.2021.111026.

[48] Y. Fan, D. Wu, S. Zhang, L. Zhang, W. Hu, C. Zhu, X. Gong, Effective photodegradation of 4-nitrophenol with CuO nano particles prepared by ionic liquids/water system, Green Chemical Engineering 3 (2022) 15–24, https://doi.org/10.1016/j.gce.2021.07.009.

[49] A. Verma, D.P. Jaihindh, Y.P. Fu, Photocatalytic 4-nitrophenol degradation and oxygen evolution reaction in CuO/g-C3N4 composites prepared by deep eutectic solvent-assisted chlorine doping, Dalton Trans. 48 (2019) 8594–8610, https://doi.org/10.1039/c9dt01046g.

[50] S. Kang, J. Jang, R.C. Pawar, S.H. Ahn, C.S. Lee, Low temperature fabrication of Fe2O3 nanorod film coated with ultra-thin g-C3N4 for a direct z-scheme exerting photocatalytic activities, RSC Adv. 8 (2018) 33600–33613, https://doi.org/10.1039/c8ra04499f.